Applied Water Science (2020) 10:76
https://doi.org/10.1007/s13201-020-1143-1

ORIGINAL ARTICLE

Photodegradation activity of yttrium-doped SnO_2 nanoparticles against methylene blue dye and antibacterial effects

Ameer Baig Ali Baig[1] · Vadamalar Rathinam[1] · Jayanthi Palaninathan[1]

Received: 14 December 2019 / Accepted: 9 January 2020 / Published online: 12 February 2020

Abstract

This review reports the effects of yttrium (Y) on the physicochemical characteristics of tin(II) dioxide (SnO_2) nanoparticles (NPs), which were efficiently synthesized via a simple hydrothermal chemical route with different doping concentrations (0, 2 and 4 at%) of Y. The structural, optical and photocatalytic properties of the as-prepared Y-doped SnO_2 (Y:SnO_2) NPs were investigated, and the results are described. X-ray diffraction (XRD) studies showed that the undoped and Y:SnO_2 NPs had a fine crystalline texture with a tetragonal structure and particle size range of 27–15 nm, although the size decreased with Y doping. High-resolution scanning electron microscopy (HRSEM) morphological analysis revealed spherical NPs forming agglomerates. Optical absorption was investigated by UV-visible diffuse reflectance spectroscopy, and showed a redshift in bandgap energy for Y^{3+}-doped SnO_2 NPs, and photoluminescence spectroscopy revealed the most intense emission peaks in the visible light region. Enhanced photocatalytic activity was observed for the doped samples, and the 4% Y:SnO_2 NPs exhibited excellent photodegradation of methylene blue aqueous (MB) dye in visible light, demonstrating 92.34% degradation in 180 min. The other photocatalysts also demonstrated greater than 85% photodegradation efficiency and high stability, with no significant reduction in activity observed after five cycles. The results indicate that the superoxide ($^{\cdot}O_2^-$) radical, a key reactive species, played a vital role in the degradation of aqueous MB dye. The probable photocatalytic mechanism of the Y:SnO_2 NPs was thoroughly investigated.

Keywords Yttrium (Y^{3+})-doped SnO_2 · Photocatalysts · Recyclability · Dye degradation · Active species · Antibacterial effects

Introduction

Point-source pollution of water bodies from organic contaminants as a result of industrial waste poses a growing threat to the world's ecosystems (Aristi et al. 2015). Numerous methods have been proposed for the removal of toxins from wastewater to limit their effect on the environment (Saleh et al. 2019). Remediation by methods such as photocatalytic treatment to remove dye toxins from wastewater is critical in order to prevent the death of aquatic animals, human disease, and destruction of ecosystems (Jayapandi et al. 2019). One of the most effective means of wastewater remediation is the use of advanced oxidation processes (AOP), and a number of methods have been reported (Bartolomeu et al. 2018). Over the previous decade, semiconductor photocatalysts (PCs) have become widely used to address a number of environmental issues such as hazardous waste remediation and energy harms utilizing abundant solar light, with the advantages of cost-effectiveness, low toxicity, recyclability, and the ability to facilitate multi-step electron transfer progressions (Xu et al. 2019). Recent efforts to develop semiconductor materials with precise size, shape, and optical, electrical, and catalytic properties has garnered attention in the areas of conservation, biosystems, and energy tenders (Ravichandran et al. 2017; Jayapandi et al. 2019). The exploitation of solar energy and photocatalysts (PCs) centered on TiO_2, ZnO and tin oxide (SnO_2) is a simple and vibrant solution to destroy and eliminate these organic impurities (Feng et al. 2015; Wang et al. 2015; Vignesh et al. 2019a). SnO_2 is chief n-type semiconductor with a wide/direct bandgap of ~ 3.6 eV (Mani et al.

✉ Ameer Baig Ali Baig
ameerramphysics@gmail.com

[1] PG & Research Department of Physics, Muthurangam Government Arts College (Autonomous), Vellore, Tamil Nadu 632 002, India

2018). Similarly, it has unique characteristics including high chemical and thermal stability, high binding energy, good optical transparency and high capacity for oxygen adsorption on its surface (Dobrucka et al. 2018; Pandiyan et al. 2019). The modification and enhancement in the adaptable and stretchy properties of SnO_2 nanostructures (NSs) are important for various applications such as lithium-ion batteries (Li et al. 2011), optoelectronic devices (Agrahari et al. 2015), gas sensors (Yang et al. 2018), transparent conductors (Lili et al. 2006), light-emitting diodes (Lee et al. 2013), solar cells (Gubbala et al. 2008), and usually photocatalysis (Bhuvaneswari et al. 2018). With regard to environmental effluence, the contaminants from organic dyes used in textile and dye industries have been recognized as a toxic substance and a growing threat throughout the world (Suthakaran et al. 2019). Methylene blue (MB), an organic dye, is used in the areas of textiles, paper fabrication and biomedicine (Soltan et al. 2017). However, the instinct bandgap of SnO_2 limits the absorption facility of visible light since under sunlight, which results in the relatively low efficiency. The photocatalytic activity generally depends on the generation of electron–hole pairs in semiconductor nanoparticles (NPs) under exposure to visible/UV light, hence hasty recombination of the photoexcited electron–hole pairs inhibits has an expansion of the photocatalytic performance (Palanisamy et al. 2018). Even though SnO_2 appears to be a favorable semiconductor material for photovoltaic applications, its photocatalytic efficiency is often limited as of poor quantum profit triggered by the fast recombination rate and ineffectual use of photoexcited electron–hole sets. To overcome this issue, an amendment is one strategy for improving light absorption, which the amalgamate of visible light-sensitive PCs might be centered on (Wu et al. 2019). The metal oxides (SnO_2) as a type of semiconductor could retain multifunctional properties via particle size distribution, changes in morphology, compound forming, doping and co-doping (Xin et al. 2012). Thus, the studies which executed to enhance the physicochemical properties of SnO_2 are indeed essential for various reasons. Several techniques have been explored to extend the absorption wavelength of SnO_2 into the visible region, including semiconductor metal doping/pairing. Exclusively in doping has modest and convenient approaches to decrease the bandgap, hence tempt and enrich several assets led to enhanced photocatalytic activity under UV to visible light (Palareti et al. 2016). Yttrium is rare earth metallic a efficient dopant, meanwhile, the surface segregation of Y^{3+} ions forms several oxygen vacancies (V_o) owns great optical conductivity which aids fast electron transfer and short work utility esteeming the realization of noble band orientation (Sanoop et al. 2016). To the best of our knowledge, the effect of yttrium (Y^{3+}) doping on the structural, optical, and photocatalytic properties of SnO_2 have not been reported thus far. Doping of Y^{3+} ion-doped/burdened into SnO_2 effectively inhibits electron–hole recombination, leading to superior photocatalytic activity under visible light and enhanced antibacterial activity.

The main profits of (1) yttrium doping might decline in band of the wide bandgap values, (2) the Y^{3+} exterior might enrichment hinders on crystallite growth then (3) variance between the oxidation state exclusion of Sn^{4+} and Y^{3+} could stimulates large defects of oxygen vacancies (V_o) in SnO_2 structure; V_o has key role in improving numerous properties (Akbari-Fakhrabadi et al. 2015; Dohcevic-Mitrovic et al. 2015). Y doping may improve the photocatalytic efficiency of SnO_2 for the above-stated reasons and, leading to improved physicochemical properties, catalytic stability, greater durability and lower cost. In the present work, hydrothermal chemical precipitation amalgamate of Y-doped SnO_2 (Y:SnO_2) NPs by different content of Y (0, 2 and 4 at%) was used to reduce MB aqueous solution under visible-light photocatalysis, and antibacterial activity was investigated and their effects are discussed in detail. Among the various chemical methods used to synthesize undoped and doped NPs, a simple chemical primed as an inexpensive way adopted here for numerous advantages such as low cost, rapid synthesis, ease of doping, and low preparation temperature.

Experimental conditions

Materials and reagents

Yttrium(III) nitrate hexahydrate $Y(NO_3)_3{\cdot}6H_2O$, sodium hydroxide (NaOH), tin(IV) chloride ($SnCl_4{\cdot}5H_2O$) pentahydrate, ethylene diamine tetraacetic acid (EDTA-2Na), 1,4-benzoquinone (BQ), isopropanol (IPA), and absolute ethanol (CH_3CH_2OH) were obtained from SDFCL Chemical Reagent Co., Pvt. Ltd., India. Methylene blue ($C_{16}H_{18}ClN_3S$) was obtained from SD Fine Chemical Co., Pvt. Ltd, and the aforesaid materials stood used for precursors. All of the standard mixtures used in this review were of analytical reagent (AR) grade and were used without further purification. Deionized (DI) water was used for all experiments.

Sample preparation

The Y:SnO_2 NPs with a softening fitting amount of yttrium (Y) dopant (0, 2 and 4%) with preparatory materials (Sn) in DI water were synthesized by a facile hydrothermal chemical precipitation method. The 0.1 M of $SnCl_4{\cdot}5H_2O$ was used as a precursor for preparing the SnO_2 NPs. The $SnCl_4{\cdot}5H_2O$ was dissolved in a solution of HCl and DI water (1:4, total volume of 50 mL). Next, NaOH solution (1 g

NaOH dissolved in 20 mL DI water) was added dropwise, under vigorous magnetic-stirring to obtain a pH value of 10 to form precipitates. To achieve water-soluble Y doping, the $Y(NO_3)_3{\cdot}6H_2O$ (Y content in the samples was 0, 2 and 4 wt%, respectively) concentration was added to the same mixture. The resulting solution was maintained under constant stirring for 6 h to determine the response, and then transferred to a Teflon-lined stainless steel autoclave and maintained at 160 °C for 24 h, after which it was cooled to room temperature. Significance the gray coloured was occupied and thoroughly washed by DI water and ethanol plumbed until free of remove Cl^- ions over testing the residual liquid, then drying in an oven at 60–70 °C. The residual product was then powdered into fine NPs with an agate mortar to obtain 2 and 4% Y:SnO_2 (yttrium-doped SnO_2) NPs for further analysis, and the same procedure was used to synthesize undoped/pristine SnO_2 NPs was adopted without the use of Y source.

Characterization

The structural properties of the crystalline phases and size of the prepared nanoparticles were evaluated by X-ray powder diffraction (XRD) analysis using a Rigaku MiniFlex II X-ray diffractometer extent over monochromatic Cu Kα radiation. Fourier transform infrared (FTIR) analysis was performed on a PerkinElmer RX1 spectrophotometer to evaluate the presence of functional groups. High-resolution scanning electron microscopy (HRSEM) is a valuable system for determining the surface morphology and particle size of the NPs, and the chemical composition is determined by elemental analysis. In order to determine whether the Y dopant was successfully doped into the unified NSs, studies were carried out by energy-dispersive X-ray spectroscopy (EDX) coupled with HRSEM (Hitachi S-3000H) The optical properties and bandgap values were obtained using a UV–Vis diffuse reflectance spectrophotometer (UV–Vis DRS; JASCO V-770 UV/Vis/NIR). Intense peaks were observed by photoluminescence (PL) spectroscopy using JASCO FP-8300 spectrofluorometer at an excitation series of ~ 272 nm.

Investigation of photocatalytic activity

The photodegradation of MB aqueous dye (20 ppm; 10 mg/L) solution by photocatalytic activity of the obtained Y:SnO_2 NPs was evaluated in 100 mL of DI water for visible light exposure under a high-pressure mercury lamp (300 W) at a constant room temperature, with 10 mg of structured samples as photocatalysts. Prior to irradiation, the mixture was stirred in the dark for 30 min to achieve adsorption–desorption equilibrium between the MB molecules and catalyst surface, and the mixture was exposed to light protection. Through the catalytic response, a variable range of dye solutions was measured and centrifuged for 10 min to eradicate the catalyst. The absorption of cleared MB dye (λ_{max} of 664 nm) solution was measured during photocatalytic capacities at 30-min intervals by a UV–Vis spectrophotometer (PerkinElmer Lambda-19). The notable absorption mechanism was conceded via IPA, BQ and EDTA in this effort remained used as the hydroxyl ($^{\cdot}OH$), superoxide radicals ($.O^{2-}$) and holes (h^+) scavengers, respectively. Four cycled were carried out to determine the stability of the photocatalyst.

Antibacterial performance

The antibacterial performance of Y:SnO_2 NPs was studied against the check organisms gram-positive (*Staphylococcus aureus*) and gram-negative (*Escherichia coliEscherichia coli*) bacterial strains were decorative via agar-well-diffusion approach, and Müller–Hinton agar was used for bacterial culture (Palanisamy et al. 2019). The plate organized for agar wells by hovering out the type with a hygienic tool was loaded with different concentrations (25, 50 and 100 µL) to obtain undoped/pristine and Y:SnO_2 twisted solution, after which these cultures were placed in a shaking incubator at 37 °C for 24 h for evolution. Likely, the negative control (dimethyl sulfoxide; DMSO) values were restrained in the alike progression. After culturing, the diameters of the zone of inhibition (ZOI) that formed around the zone wells were examined and renowned and the ZOI are itemized as the mean ± typical deviation.

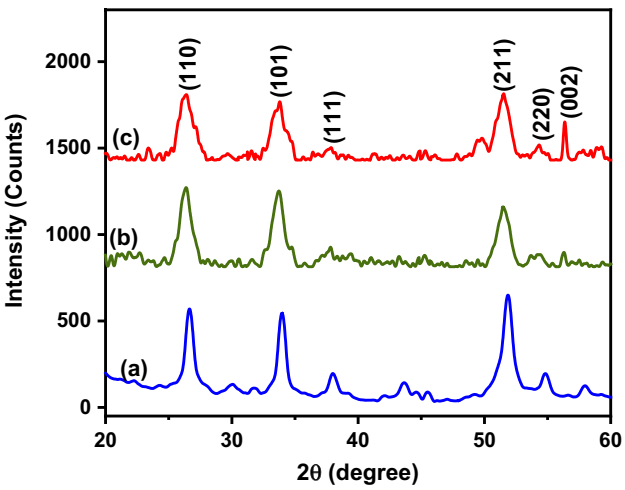

Fig. 1 XRD patterns of (a) SnO_2, (b) 2% Y-doped SnO_2 and (c) 4% Y-doped SnO_2 NPs

Results and discussion

Figure 1 shows the XRD patterns of the undoped and the 2% and 4% Y-doped SnO_2 NPs. All diffraction peaks obtained were perfectly ascribed to tetragonal rutile SnO_2 crystalline phase by space group P42/mnm (JCPDS card file no. 41-1445) (Li et al. 2019). For these SnO_2 samples, the intense peaks observed at $2\theta = 26.65°$, 33.97°, 38.01°, 51.85°, 54.83° and 57.97° were accurately assigned to the lattice planes (110), (101), (111), (211), (220) and (002) of tetragonal SnO_2, respectively (Wang et al. 2019). Doped SnO_2 samples presented similar patterns without substantial diffraction peaks since any impurity phases possibly for the content of Y or their oxides, compatible the sole phase nature, great pureness and proposed the active integration of Y dopants would be consistently replaced into SnO_2 host lattice/interstitial sites which suggests to deficiency in crystals were fine crystallized. Likewise, the as-prepared Y:SnO_2 samples clearly showed strong preferential growth along the (110) plane which through reduced/shifted the diffraction peak intensity to a lower diffraction angle and also converted more widened which might be owing to the aggregate the Y concentration. Additionally, Y doping inhibited grain growth and lattice distortion resulting from the Y^{3+} ion substitution for Sn^{4+}, which may produce oxygen vacancies. The crystallite sizes of the undoped and the 2% and 4% Y-doped SnO_2 NPs were assessed using the interplanar spacing Scherrer equation (Manjula and Selvan 2017), $d = 0.89\lambda/\beta\cos\theta$, where 0.89 is Scherrer's constant, θ is the Bragg diffraction angle, λ is the X-ray wavelength, and β is the full width at half maximum (FWHM) of the diffraction peaks. The decrease in particle size might be knowingly inhibited owing to occurrence of Y^{3+}. The main reason was that the ionic radius of Y^{3+} (0.086 nm) was longer than that of Sn^{4+} (0.069 nm) (Jayapandi et al. 2019).

FTIR spectroscopy

FT-IR spectroscopy is credibly the supreme leading device for recognizing the functional groups or the kinds of chemical links. FT-IR spectra of undoped, 2% and 4% Y-doped SnO_2 NPs are shown in Fig. 2. The as-obtained SnO_2 NPs essentially revealed two absorption bands at 3552 and 1637 cm^{-1} which were attributed to stretching and bending vibrations of the surface hydroxyl group (–OH) associated with the adsorbed/re-adsorbed water on the SnO_2 surface at ambient temperature, respectively (Suthakaran et al. 2019). The strong absorption group present in the lower-wavenumber region (600–800 cm^{-1}) chiefly at 476 and 627 cm^{-1} signifies the typical IR bands of doped SnO_2

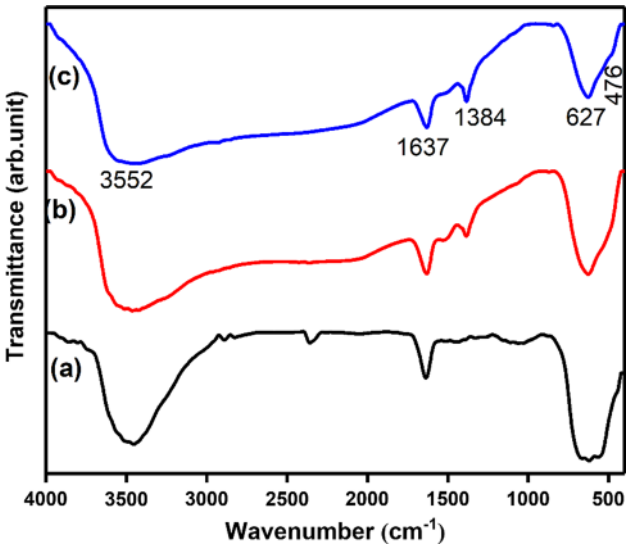

Fig. 2 FTIR spectra of (a) SnO_2, (b) 2% Y-doped SnO_2 NPs and (c) 4% Y-doped SnO_2 NPs

samples structure assigned to metal–oxygen for anti-symmetric O–Sn–O and Sn–O (terminal oxygen vibration of Sn–OH) lattice extending vibrations, respectively (Manjula and Selvan 2017; Dobrucka et al. 2018). Excluding these bands, no further absorption processes were detected, indicating consistent dispersal of dopants ions and the great clarity for the as-blended samples, henceforth the shifts to lower wavenumber might be construed by a variation in the bond length or asset of Sn^{4+} and O_2^- bond (Phukan et al. 2017). The strong bands linked to $^-$OH groups indicate that these samples may achieve high photocatalytic activity. In photocatalysis, the primary mechanism of photodegradation is typically by the hydroxyl radicals ($^-$OH$^\bullet$), which can be formed through the response of $^-$OH groups present on the NPs with the generated holes.

Morphological and compositional studies

Figure 3a displays the HR-SEM micrographs of 4% Y:SnO_2 NPs. The sample has visibly presented the surfaces perform to be dopant of grains although exact fine nanoparticles by the spherical made grade of agglomeration morphologies and identical crystallites spreading, however, supposed to be an imperative aspect in photocatalytic response. The EDX spectrum (Fig. 3b) disclosed the general presence of Sn, O and Y elements and witnessed values (wt%) with the non-existence of some other elements, authorizing its purity and accessibility in authenticating the efficacious integration of Y dopant on to SnO_2 matrix. All the elements are located in different colours in different area are shown in Fig. 4.

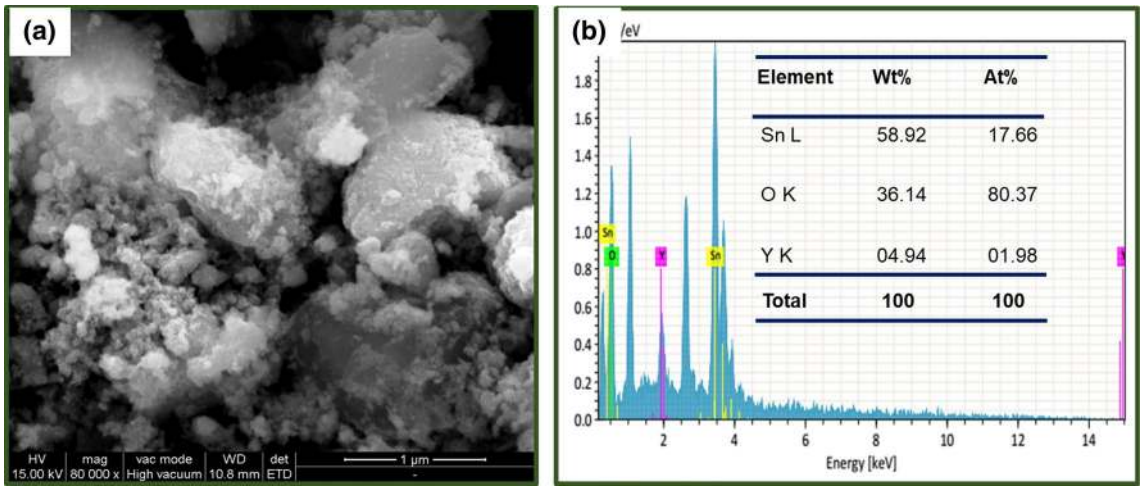

Fig. 3 **a** HR-SEM image and **b** EDX spectra of 4% Y-doped SnO_2 NPs

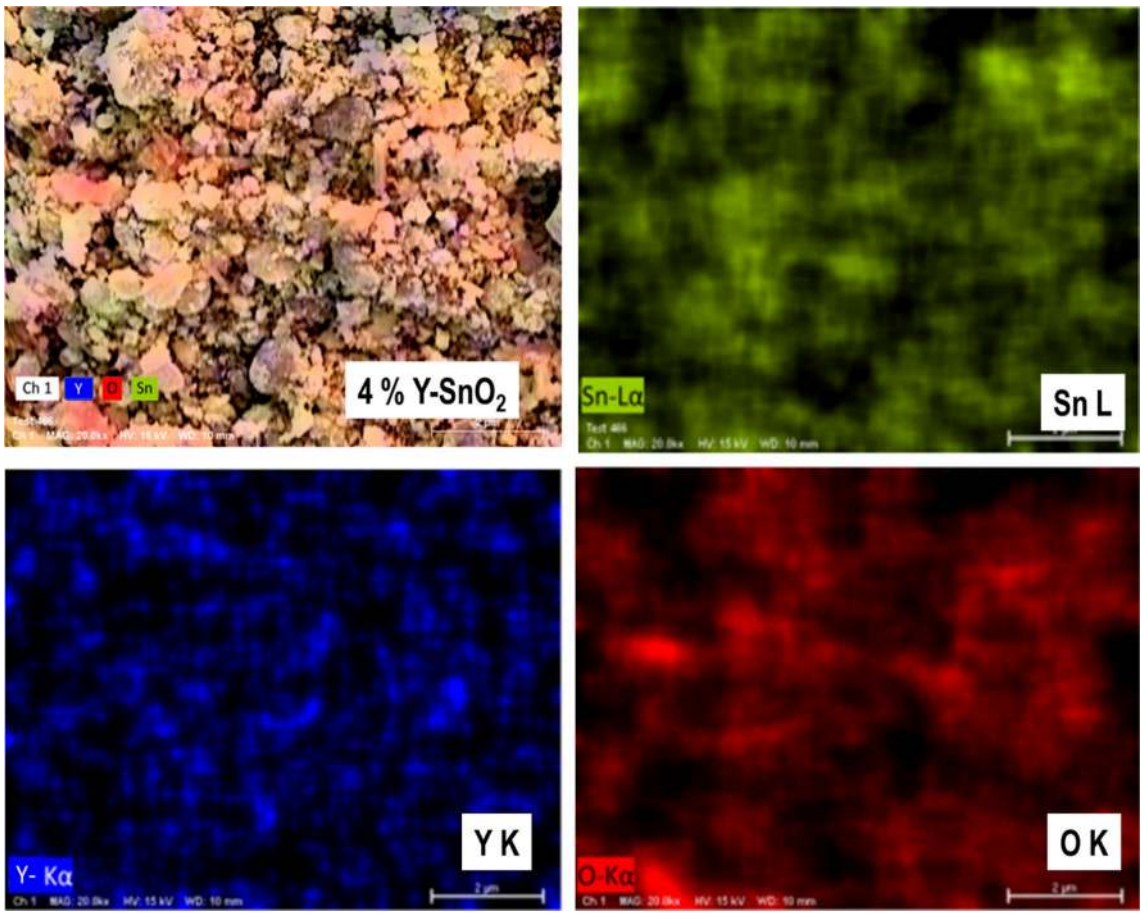

Fig. 4 EDX elemental mapping of 4% Y-doped SnO_2 NPs

Optical properties

The effect of Y doping on the optical properties and bandgap of the as-prepared undoped, and 2 and 4% Y-doped SnO_2 NPs was determined by an exact adaptable procedure of UV-DRS absorption spectroscopy. Figure 5A indicates of all the as-obtained samples extant a worthy optical eminence in UV–Vis region then the solid absorbance in the series of

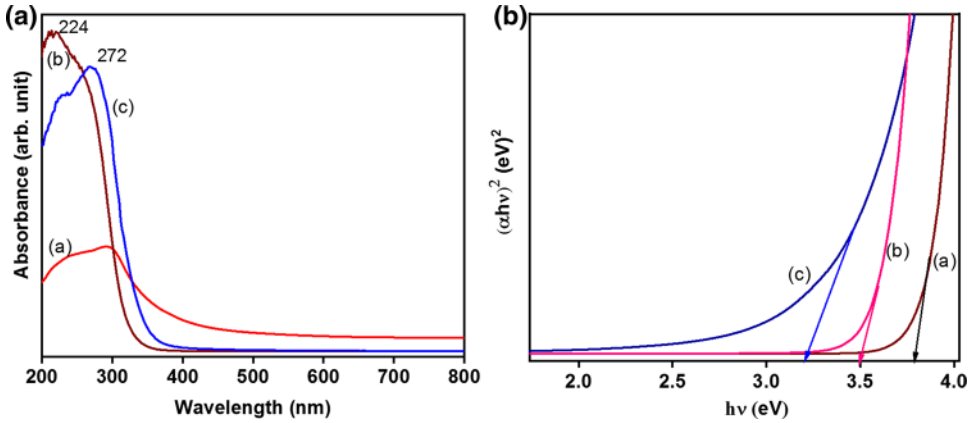

Fig. 5 **A** UV spectra and **B** Bandgap energy of (a) SnO_2, (b) 2% Y-doped SnO_2 NPs and (c) 4% Y-doped SnO_2 NPs

~220–272 nm. A sharp absorption edge nearby 272 nm was spotted for 4% Y-doped SnO_2 NPs owed to fairly large exciton binding energy though distinctive of cassiterite SnO_2. In red-shift of the absorption edges by growing the Y doping concentration analogous to the Fermi level shifts with an upturn in the carrier concentration besides owed toward quantum confinement influence (Palareti et al. 2016). This tendency is usually ascribed to charge transfer progressions from the valence band (VB) of SnO_2 to the energy near of Y^{3+} ions that are sited fair lower the conduction band (CB) of SnO_2 (Sanoop et al. 2016). To acquire a further assessable vision in this conduct, the bandgap energy (E_g) values of the as-obtained samples were done by inferring the linear part of $h\nu$ versus $(\alpha h\nu)^2$ graph diverts of the x-axis according to the Tauc equation (Palanisamy and Pazhanivel 2018; Sujatha et al. 2019), as shown in Fig. 5B, where α, A, $h\nu$, E_g, and n ($n = 2$ or 1/2 for allowed indirect or direct conversion) are the absorption coefficient (or optical density), a constant, photon energy, bandgap energy, and parameter fitting to the nature of semiconductor, respectively. The bandgap energies declined since 3.79 eV for undoped SnO_2 to 3.49 and 3.2 eV for 2% and 4% Y-doped SnO_2 NPs, respectively, consistent to wavelength occurs/fortunate in the visible region range. It could be detected that the E_g value lessened steadily with increasing the yttrium (Y^{3+}) concentration, henceforth the decline in the bandgap energy was modernized via electronic construction and proposing an *s–d* and *p–d* exchange interfaces in d-band electrons (e^-) of the Y^{3+} ions exchanged on the Sn sites of the host SnO_2 medium (Jayapandi et al. 2019). The CB in the SnO_2 samples mostly comprise Sn5*s*, Sn5*p*, and O_2 states, although the VB was essentially calm through O_2p states. The lower E_g of the semiconductor results in an increase in photon gathering, photoreactive and inhibiting the electron–hole recombination, leading to the higher photocatalytic activity of the 4% Y-doped SnO_2 NPs than the other nanomaterials (NMs). The bandgap engineering by quantum size upshot is originated to be beneficial for changing the efficiency of photocatalytic response.

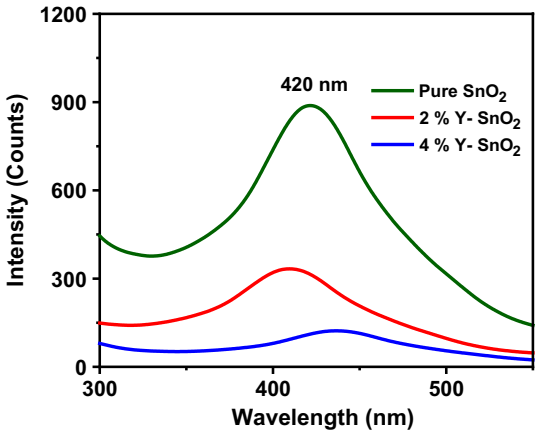

Fig. 6 PL spectra of (a) SnO_2, (b) 2% Y-doped SnO_2 NPs and (c) 4% Y-doped SnO_2 NPs

Photoluminescence (PL) spectra analysis

PL spectroscopy was used to investigate the surface defects, impurities, energy bands, and exciton assembly of the as-obtained NMs. Figure 6 displays the room-temperature PL spectra of Y:SnO_2 NPs by an excitation wavelength of ~272 nm. A wide-ranging emission performed at 452 nm (blue emission) in all achieved samples are instigate via band–band owed to the profound level or traps state emissions, electronic transitions, surface defects since the Sn interstitials and/or interstitial V_o level. Hence, the recombination of the photoexcited electron from the CB and hole in the VB has declined intensity to greater level exciton emission allied to quantum detention were witnessed. And the spectral emission group associated to dispensed by direct recombination of free exciton recombination from the near conduction band edge (NCBE) to near valence band edge (NVBE), i.e., electron of Sn 4*p* CB and hole in the O_2p of the VB (Palareti et al. 2016). The results suggest that Y doping might decrease the E_g of SnO_2 and promote photo-response

capability, producing a large number of active sites inside the SnO_2 while between VB and CB by Y^{3+} ion exchange as well. This indicates that the great separation prospect among the photoexcited electron–hole recombination is slightly declined steadily peak intensity, which grades in the realization of reactive surface interiors instigated via additional Y^{3+} for enhancing photodegradation efficiency.

Photocatalytic performance and carrier concentration

The photocatalytic activity/discolouration of as-prepared Y:SnO_2 NPs was surveyed by oxidative of the reactive MB aqueous dye in visible light revelation. Figure 7a shows that the MB dye distinct absorption peak gradually decreased with increasing visible light time in united with 10 mg of PCs for 180 min, and the accumulation of Y:SnO_2 PCs caused an apparent degradation of MB dye. In the absence of a catalyst, the variation in absorbance of MB solution was negligible. The 4% Y:SnO_2 PCs essentially displayed an enhanced photocatalytic activity likened to that of undoped

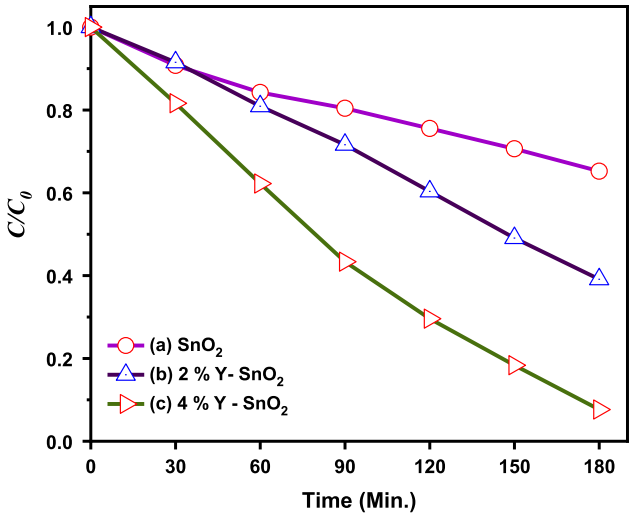

Fig. 8 Photocatalytic degradation of MB (a) SnO_2, (b) 2% Y-doped SnO_2 NPs and (c) 4% Y-doped SnO_2 NPs

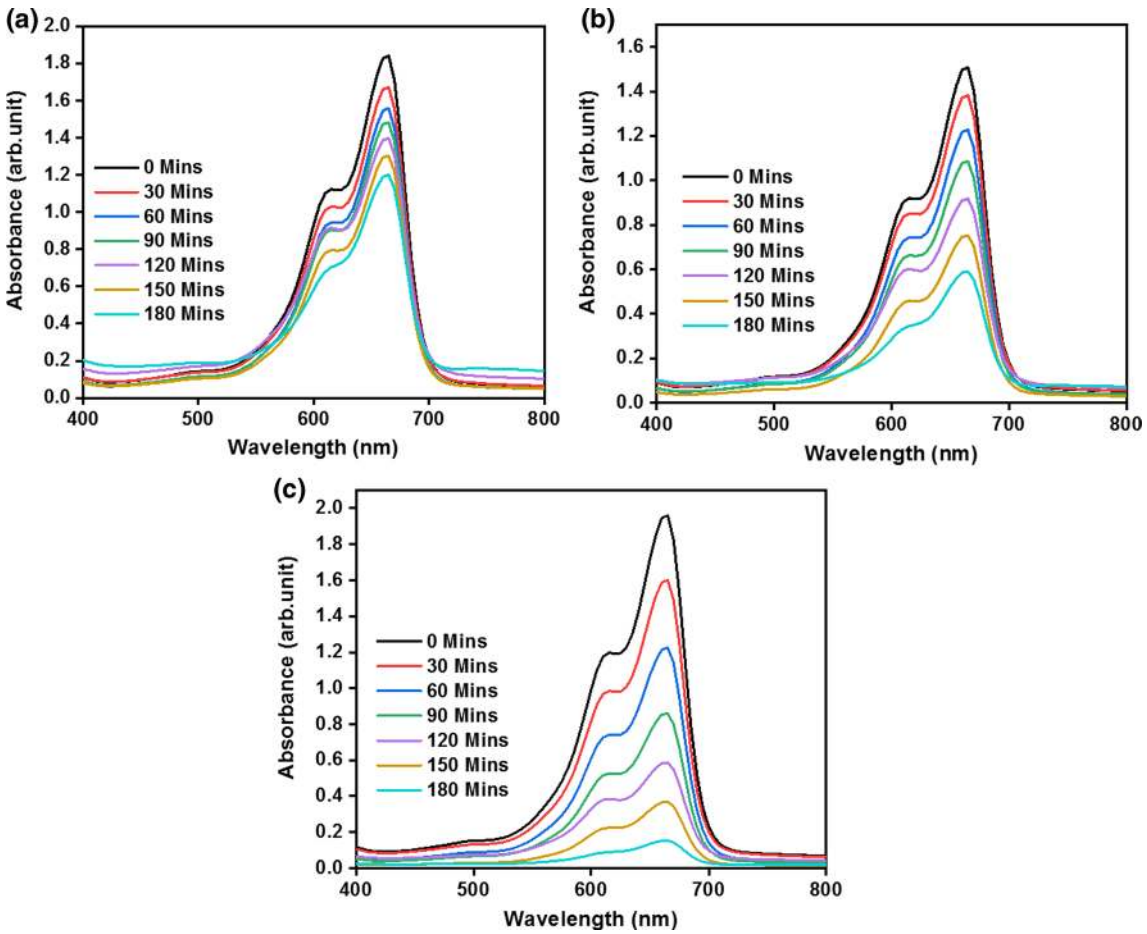

Fig. 7 UV–visible absorption spectra for MB degradation by samples of **a** SnO_2, **b** 2% Y-doped SnO_2 NPs and **c** 4% Y-doped SnO_2 NPs

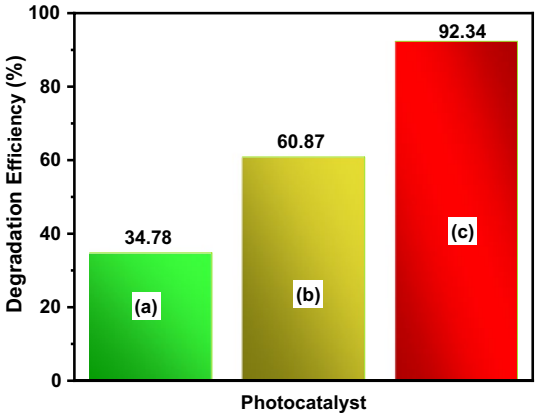

Fig. 9 Degradation efficiency of MB for (a) SnO_2, (b) 2% Y-doped SnO_2 NPs and (c) 4% Y-doped SnO_2 NPs

and 2% Y:SnO_2. The photodegradation rate (%) of MB solution at different time periods for all as-obtained conformations through distinct as C/C_0 was calculated and is displayed in Fig. 8, where C_0 is the initial concentration of the MB solutions (mg/L), and C_t is the concentration of the MB dye after a specified time period. The photodegradation of the MB dye was 34.78, 60.87, and 92.34% for the undoped and the 2% Y:SnO_2 and 4% Y:SnO_2 PCs, respectively, under visible light exposure for 180 min (Fig. 9). It can be seen that the photodegradation efficiency of SnO_2 was improved by Y^{3+} doping, and the 4% Y-doped SnO_2 photocatalyst samples exhibited the highest efficiency of 92.34%. These results permit us to conclude that 4% Y:SnO_2 NPs are effective photoactive materials, with significant dye adsorption on the surface. The concentration of 4% Y was found to be optimal, showing superior light absorption, hereafter to evidently directed the photocatalytic performance of SnO_2 NPs. It could be realized that Y:SnO_2 NPs demonstrated the highest efficiency at entire interval time by enhanced activity of 92.34% after 180 min. The movement for MB photodegradation followed the order 4% Y:SnO_2 > 2% Y:SnO_2 > SnO_2.

To further assess the photocatalytic efficiency of the undoped and Y-doped SnO_2 PCs, a kinetic analysis of MB dye removal was carried out. As revealed in Fig. 10, the photodegradation of MB dye through Y:SnO_2 PCs surveyed a pseudo-first-order rate law, $\ln(C_t/C_0) = -k_{app}t$, where k_{app} is the negative rate constant of the removal. It could be visibly appreciated that the reaction rates of 4% Y:SnO_2 sample remained superior to that of as-obtained undoped SnO_2. Specifically, the 4% Y:SnO_2 sample demonstrated the highest catalytic activity, with an obvious rate constant of 0.0123 min^{-1} for MB dye degradation, which was around 5.59 times that of undoped SnO_2 (0.0022 min^{-1}).

The recyclability of the 4% Y:SnO_2 photocatalyst was investigated to determine its stability and recyclability for potential application (Senasu et al. 2018; Vignesh et al. 2018). After photodegradation of MB dye for 180 min, the sample was strained and the 4% Y:SnO_2 PCs is washed by centrifuge with DI water and then dried in an oven for next recycle progression. The recovered 4% Y:SnO_2 PCs was exposed to four cycles of MB dye in visible light for up to 12 h, and the stable degradation efficiency is displayed in Fig. 11. For the third and fourth cycles, the degradation efficiency of 4% Y:SnO_2 PCs was 89% and 85%, respectively. The photocatalytic productivity of the recycled samples indicates only a minor decline up to five recycles, which verifies that productivity of the photocatalyst has reasonably unaffected for use of four recycles. This small difference in efficiency may be attributed to

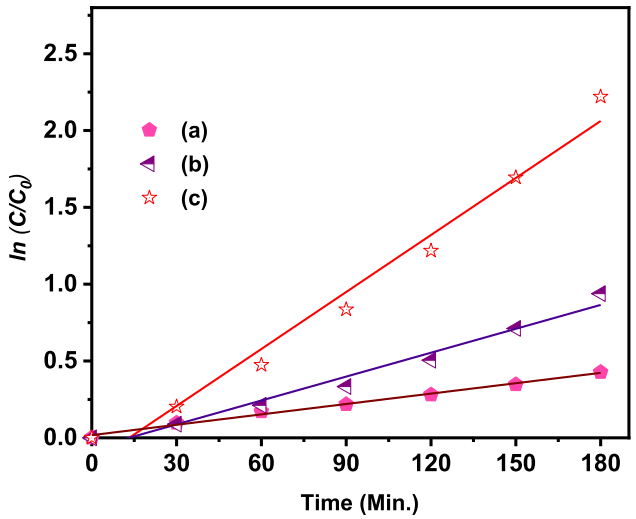

Fig. 10 First-order kinetics plot for the degradation of MB on (a) SnO_2, (b) 2% Y-doped SnO_2 NPs and (c) 4% Y-doped SnO_2 NPs

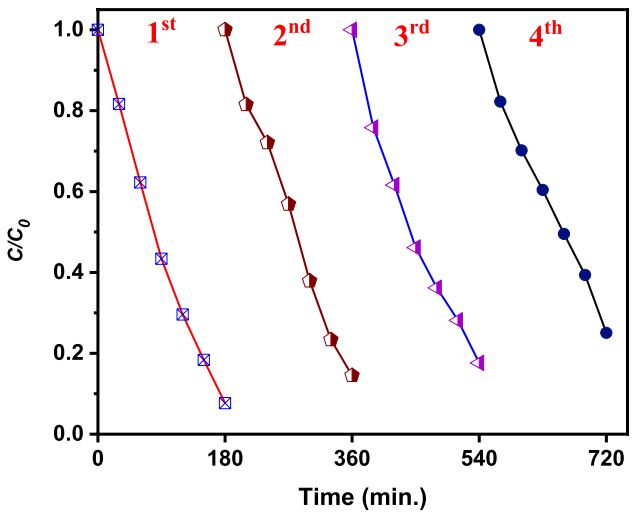

Fig. 11 Four repeated processes of 4% Y-doped SnO_2 NPs for photodegradation of MB under UV–visible light irradiation

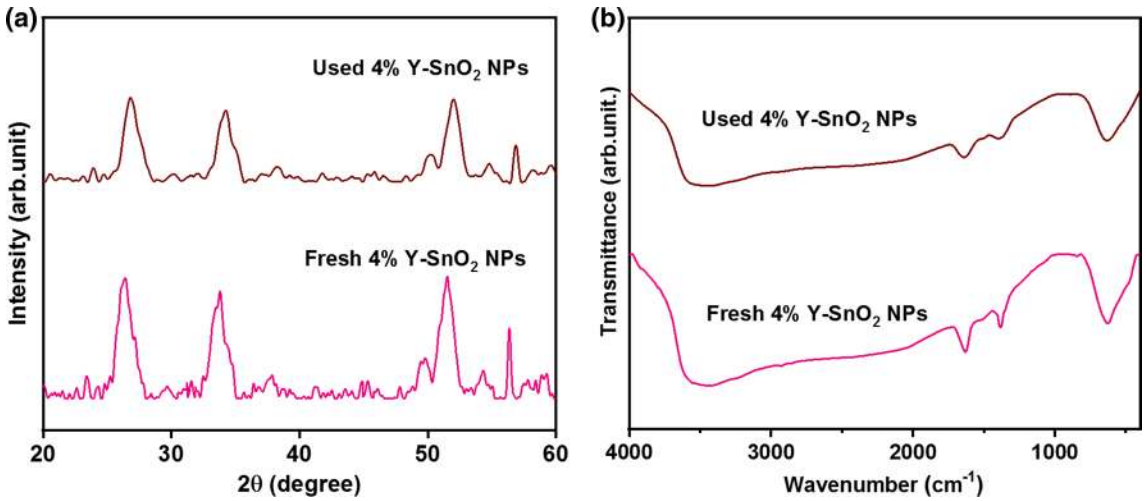

Fig. 12 XRD pattern and FTIR spectra for 4% Y-doped SnO_2 NPs fresh and used photocatalytic reaction

Table 1 Comparison of visible light generated MB degradation rate (%) over of previously reported nanomaterials

S. no.	Photocatalyst	Dye	Irradiation time (min)	Degradation efficiency (%)	References
1.	Bistructural SnO_2 nanobelts	MB	300	~78.4	Wang et al. (2018)
2	Ferroelectric $Li_{1-x}Ta_{1-x}W_xO_3$ materials ($x=0$ to 0.25)	MB	360	~95	Benzaouak et al. (2018)
3	White zirconia nanoparticles	MB	300	~76	Teeparthi et al. (2018)
4	$CdFe_2O_4$ nanoparticles	MB	300	~90	Patil et al. (2018)
5	ZnO–SnO_2 nanocomposite	MB	240	~91	Rashad et al. (2014)
6	P-25 TiO_2 nanoparticles	MB	360	~47	Sangchay et al. (2012)
7	4% Y-doped SnO_2 NPs	MB	120	~92.34	This work

the imperfect recollection (i.e.) loss of certain nanopowders in the washing process and high resistance of the PCs to photo-corrosion. Likewise, the XRD pattern and FTIR spectra of earlier and later MB dye degraded 4% Y:SnO_2 PCs are displayed in Fig. 12, which shows the genuine crystalline structure and leading functional decontamination after photodegradation. The results validate that the capable photocatalytic concert of 4% Y:SnO_2 PCs sample consuming extended time stability and recycling capability is fortunate in excellent photocatalytic performance suitable for environmental use. This progress respites the photocatalytic activity might also increase since the coupling of NMs with dissimilar bandgap supporting the electron–hole charge separation as in the instance of metal oxide (MO) per several heterojunctions. The photocatalytic performance of the as-prepared 4% Y:SnO_2 PCs was compared with recently reported PCs with different semiconductor metal oxides/metal and auxiliary nanocomposites, as shown in Table 1 (Rashad et al. 2014; Wang et al. 2018; Patil et al. 2018; Benzaouak et al. 2018; Teeparthi et al. 2018).

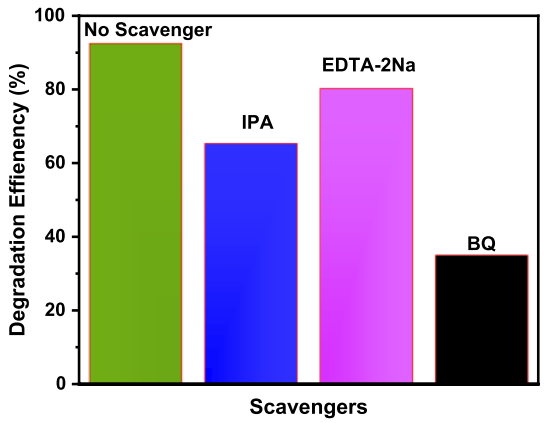

Fig. 13 Effects of different scavengers on the degradation of MB dye in the presence of 4% Y-doped SnO_2 NPs

Photodegradation mechanism

To further elucidate the likely mechanism of photocatalysis surface could be recognized, the responsive species and

the trapping trials/interiors (Vignesh et al. 2019b) were performed as presented in Fig. 13 When BQ is hosted, the substantial decrease in photocatalytic degradation efficiency arises, designating $O_2{\cdot}^-$ is the decisive energetic species donating to the degradation response. Conversely, by adding IPA and EDTA-2Na, the degradation competence could slightly deviations, its proposing $^-OH^{\cdot}$ and h^+ radicals are incidentally consumed (i.e.) not the chief reactive kinds in the photocatalytic coordination of 4% Y:SnO_2 NPs. In visible light irradiation, electrons in the VB of catalyst could empower to transference to the CB; electron–hole pairs were created (Bhuvaneswari et al. 2019). Once light exposes on Y:SnO_2 PCs surface, it makes electron–hole pairs arrive in chemical response to custom exact reactive species. Moreover, the visible light irradiation on the surface of the Y^{3+}-doped SnO_2 catalyst effectively crops electron–hole by reduction and oxidation throughout the photocatalytic reaction of SnO_2 NPs (Sanoop et al. 2016). In fact, the holes and electrons formed in the VB may respond with water (H_2O) or hydroxide ions ($^-OH^{\cdot}$) were adsorbed on Y:SnO_2 apparent, making hydroxyl radicals ($^-OH^{\cdot}$) which assist in the dynamic degradation of the MB dye solution. The electron located in the CB could interact with the adsorbed/dissolved oxygen (O_2) molecules to produce superoxide radicals ($O_2{\cdot}^-$) and H_2O_2, which could increase photocatalytic efficiency since $O_2{\cdot}^-$ is the chief active species. Furthermore, the doped Y^{3+} ions demonstrate a key role in decreasing the bandgap, ensue as traps inside in SnO_2 lattice and interruption or inhibition of the recombination of photoexcited electron and hole charge carriers, accordingly enhancing the photocatalytic activity and stability/recyclability of the catalyst. Based on the above experimental values, the likely photocatalytic mechanism is depicted in Fig. 14. Consequently, the $^-OH^{\cdot}$, $O_2{\cdot}^-$ and H_2O_2 as reactive species have the direct oxidation capability to destroy the organic compound/dyes to trivial non-harmful molecules (H_2O, CO_2). The high activity of 4% Y:SnO_2 NPs as photocatalyst could be elucidated based on the interior traps and oxygen vacancies (V_o) formed in SnO_2 by Y doping. In this construction of h^+ in the VB of Y:SnO_2 NPs has certainly probable under visible light excitation, while Y^{3+} ions adjust energy levels in the bandgap, similarly improving the charge transfer facility. In this work, Y as dopant plays a key role in tuning the optical, photocatalytic and antibacterial properties of SnO_2 NPs. The process by which the electron–hole pairs are generated from the SnO_2 PCs under visible light treatment can be described by the following steps:

$$\mathrm{Y:SnO_2 + Dye + Light \rightarrow Y:SnO_2 + Dye + \left(e^-(CB) + h^+(VB)\right)} \quad (1)$$

$$\mathrm{Dye + OH \rightarrow OH^{\cdot -} + Degradation\ Products} \quad (2)$$

$$\mathrm{Dye + O_2 \rightarrow O_2^{-} + Degradation\ Products} \quad (3)$$

$$\mathrm{O_2 \rightarrow e^-(CB) + 2h^+ + H_2O_2} \quad (4)$$

$$\mathrm{Dye + h^+(VB) \rightarrow Oxidative\ Products} \quad (5)$$

$$\mathrm{Dye + e^-(CB) \rightarrow Reduction\ Products} \quad (6)$$

Antibacterial activity of the samples

It can now be established that the bactericidal effects against *E. coli* and *S. aureus* wonders and the growth were measured, therefore owing to adsorption–desorption and physicochemical aptitudes towards the microbes, chief reason in dissimilar antibacterial activity (Shanmugam et al. 2018). It was established that the minimum inhibitory concentration

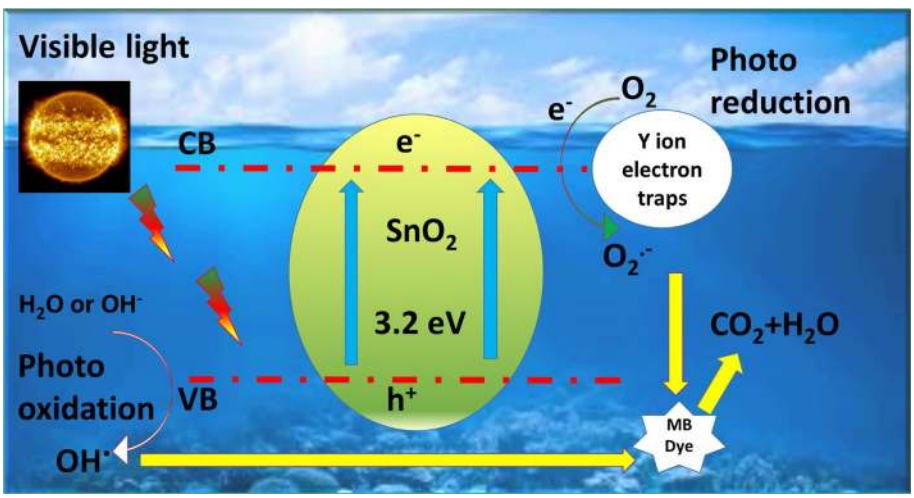

Fig. 14 The possible mechanism of MB dye degradation for 4% Y-doped SnO_2 NPs

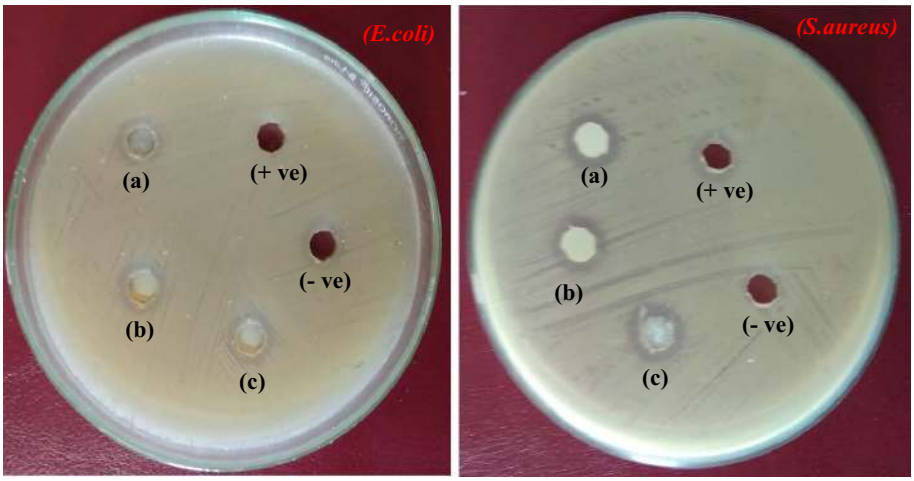

Fig. 15 Zone of inhibition test for 100 µL of (a) SnO_2, (b) 2% Y-doped SnO_2 NPs and (c) 4% Y-doped SnO_2 NPs towards *E. coli* and *S. aureus* bacteria

Table 2 Assessment of zone of inhibition of antibacterial activity for 100 µL of as-prepared nanoparticles

S. no.	Microorganisms	Zone of inhibition range (mm)	
		E. Coli.	*S. aureus*
1	SnO_2 NPs	4 ± 0.5	2 ± 0.5
2	2% Y-doped SnO_2 NPs	6 ± 1	3.5 ± 1
3	4% Y-doped SnO_2 NPs	8 ± 0.3	6 ± 0.5

(MIC) at which the bactericidal effect begins is 25 µL, and the crystal size decreased and then formerly the antibacterial activity tended to increase. Figure 15a, b shows the results of the antibacterial testing of Y:SnO_2 NPs against gram-negative (*E. coli*) and gram-positive (*S. aureus*) bacteria for various concentrations, and the ZOI diameters for all of the samples are compared in Table 2. Based on the values from the antibacterial analysis, the 4% Y:SnO_2 NPs (100 µL) exhibited a larger ZOI than the undoped and 2% Y:SnO samples. The undoped/pristine SnO_2 NPs showed the smallest antibacterial activity, due to the small concentration of the as-prepared NPs evident in the *E. coli* and *S. aureus* bacterial strains. However, with the highest doping concentration (4%) of Y in SnO_2 NPs, the ZOI was clearly observed. As the doping concentration of Y increased, the ZOI was similarly increased, so the enhanced antibacterial activity as a function of Y doping, charge density on the cell surface apparently strongly determined whether the bacteria were inhibited by Y. The accumulation of NPs on the surface of the microbes led to the disruption of cell membranes (i.e.) interfering intense to the reserve of NPs interruptions and ultimately to cell death (Ayeshamariam et al. 2015). Here, it is clear from the results that the enhanced antimicrobial properties from Y doping of SnO_2 PCs and the surface characteristics of the bacterial cell wall are closely related. Likewise, this contingent on their small particle size, poorer bandgap values of NPs, lower catalytic activity and efflux mechanism primary to the discharge of integral ions to the surface of bacteria via shortest or electrostatic powers could remain bactericidal. Equally, the discovery of reactive oxygen species (ROS), explicitly profit of superoxide anion ($-O_2^-$), hydrogen peroxide (H_2O_2) and hydroxyl radicals ($^-OH^\cdot$) on the surface of the SnO_2 NPs might enter the cell tissue. In addition, the adsorbed Y-doped SnO_2 NPs would result in grander cooperate in the structure of cell wall and interrupt in the permeability of the cell tissue and respiration system of the bacteria, leading to their death. An alternative cause of cell death is the destruction of the interior cell structure by the contact of Y^{3+} with the reactive oxygen species (ROS) formed by cells (Amininezhad et al. 2015). With the excellent bactericidal properties and stability of Y:SnO_2 NPs, they have significant potential for application in the field of antiseptic/antibiotic and biomedicine.

Summary and conclusions

To summarize, Y-doped SnO_2 NPs were successfully synthesized by a simple hydrothermal chemical precipitation process. XRD confirmed the identical integration of Y^{3+} ions into the host SnO_2 lattice without generating any inferior phases, and the typical crystal size of Y:SnO_2 decreased as the Y content increased. HRSEM interprets that spherical NPs with identical dispersal were molded in 4% Y:SnO_2 sample then similarly EDX analysis confirmed that Y was functioning assimilation into the Sn/O host lattice. The UV–Vis DRS absorption edge shifted towards the visible light region, and a notable decrease in the bandgap of SnO_2 by Y doping was observed, which is due to the realization of additional energy positions in the bandgap of SnO_2. PL analysis revealed that Y united SnO_2 NPs consume a controlled the photo-excited electron–hole separation rate and it has conveyed the sophisticated surface active sites with

oxygen deficit which were used to enhance the photocatalytic performance. High photocatalytic efficiency (92.34%) with good stability for MB dye removal was achieved with 4% Y:SnO_2 PCs with associated with undoped SnO_2 under visible light irradiation was observed. A promising photodegradation mechanism is proposed based on these findings, whereby $O_2{\cdot}^-$ are the critical robust species contributing to the degradation response. A decent antimicrobial review of Y-doped SnO_2 was explored beside gram-positive and gram-negative bacterial straining related, and so the as-obtained 4% Y:SnO_2 NPs have established that they are potentially useful for bioremediation applications. The 4% Y:SnO_2 PCs achieved an effective visible light photoreaction, displaying efficient MB photodegradation and good reusability, and thus may represent a promising alternative material for application in wastewater treatment with the evolution of clean energy.

Funding The authors received no specific funding for this work.

Compliance with ethical standards

Conflict of interest The authors declare that they have no conflict of interest.

References

Agrahari V, Mathpal MC, Kumar M, Agarwal A (2015) Investigations of optoelectronic properties in DMS SnO_2 nanoparticles. J Alloys Compd 622:48–53. https://doi.org/10.1016/j.jallcom.2014.10.009

Akbari-Fakhrabadi A, Saravanan R, Jamshidijam M et al (2015) Preparation of nanosized yttrium doped CeO_2 catalyst used for photocatalytic application. J Saudi Chem Soc 19:505–510. https://doi.org/10.1016/j.jscs.2015.06.003

Amininezhad SM, Rezvani A, Amouheidari M et al (2015) The antibacterial activity of SnO_2 nanoparticles against *Escherichia coli* and *Staphylococcus aureus*. Zahedan J Res Med Sci 17:e1053. https://doi.org/10.17795/zjrms-1053

Aristi I, von Schiller D, Arroita M et al (2015) Mixed effects of effluents from a wastewater treatment plant on river ecosystem metabolism: subsidy or stress? Freshw Biol 60:1398–1410. https://doi.org/10.1111/fwb.12576

Ayeshamariam A, Sankaracharyulu GV, Kashif M et al (2015) Antibacterial activity studies of Ni and SnO_2 loaded Chitosan beads. Mater Sci Forum 832:110–122. https://doi.org/10.4028/www.scientific.net/MSF.832.110

Bartolomeu M, Neves MGPMS, Faustino MAF, Almeida A (2018) Wastewater chemical contaminants: remediation by advanced oxidation processes. Photochem Photobiol Sci 17:1573–1598. https://doi.org/10.1039/c8pp00249e

Benzaouak A, Ellouzi I, Ouanji F et al (2018) Photocatalytic degradation of Methylene Blue (MB) dye in aqueous solution by ferroelectric $Li_{1-x}Ta_{1-x}W_xO_3$ materials. Colloids Surf A Physicochem Eng Asp 553:586–592. https://doi.org/10.1016/j.colsurfa.2018.06.011

Bhuvaneswari K, Bharathi RD, Pazhanivel T (2018) Silk fibroin linked Zn/Cd-doped SnO_2 nanoparticles to purify the organically polluted water. Mater Res Express 5:24004. https://doi.org/10.1088/2053-1591/aaaa35

Bhuvaneswari K, Palanisamy G, Pazhanivel T et al (2019) Photodegradation activity of nitrogen-rich graphitic carbon nitride intercalated ZnO\Mg–Al layered double hydroxide ternary nanocomposites on methylene blue dye. ChemistrySelect 4:2982–2990. https://doi.org/10.1002/slct.201900146

Dobrucka R, Dlugaszewska J, Kaczmarek M (2018) Cytotoxic and antimicrobial effect of biosynthesized SnO_2 nanoparticles using *Pruni spinosae* flos extract. Inorg Nano-Met Chem 48:367–376. https://doi.org/10.1080/24701556.2019.1569054

Dohcevic-Mitrovic ZD, Paunović N, Matović B et al (2015) Structural dependent room-temperature ferromagnetism in yttrium doped HfO_2 nanoparticles. Ceram Int 41:6970–6977. https://doi.org/10.1016/j.ceramint.2015.02.002

Feng S, Wang M, Zhou Y et al (2015) Double-shelled plasmonic Ag–TiO_2 hollow spheres toward visible light-active photocatalytic conversion of CO_2 into solar fuel. APL Mater 3:104416. https://doi.org/10.1063/1.4930043

Gubbala S, Chakrapani V, Kumar V, Sunkara MK (2008) Band-edge engineered hybrid structures for dye-sensitized solar cells based on SnO_2 nanowires. Adv Funct Mater 18:2411–2418. https://doi.org/10.1002/adfm.200800099

Jayapandi S, Premkumar S, Lakshmi D et al (2019) Reinforced photocatalytic reduction of SnO_2 nanoparticle by La incorporation for efficient photodegradation under visible light irradiation. J Mater Sci Mater Electron 30:8479–8492. https://doi.org/10.1007/s10854-019-01168-5

Lee H, Kang CM, Park M et al (2013) Improved efficiency of inverted organic light-emitting diodes using tin dioxide nanoparticles as an electron injection layer. ACS Appl Mater Interfaces 5:1977–1981. https://doi.org/10.1021/am302787y

Li J, Zhao Y, Wang N, Guan L (2011) A high performance carrier for SnO_2 nanoparticles used in lithium ion battery. Chem Commun 47:5238–5240. https://doi.org/10.1039/c1cc10542f

Li Y, Tang X, Zhang B, et al (2019) Electrospun Ag-doped SnO_2 hollow nanofibers with high antibacterial activity. BiorxivOrg

Lili L, Liming M, Xuechen D (2006) Solvothermal synthesis and characterization of Sb-doped SnO_2 nanoparticles used as transparent conductive films. Mater Res Bull 41:541–546. https://doi.org/10.1016/j.materresbull.2005.09.011

Mani R, Vivekanandan K, Jegatheesan A (2018) High performance photocatalytic activity of pure and Ni doped SnO_2 nanoparticles by a facile wet chemical route. J Mater Sci Mater Electron 29:6308–6315. https://doi.org/10.1007/s10854-018-8610-6

Manjula N, Selvan G (2017) Magnetic and antibacterial properties of Zr-doped SnO_2 nanopowders. J Mater Sci Mater Electron 28:15056–15064. https://doi.org/10.1007/s10854-017-7380-x

Palanisamy G, Pazhanivel T (2018) Investigation on the photophysical properties of tungsten trioxide and tungstate based nanocomposites. Mater Res Express 5:44001. https://doi.org/10.1088/2053-1591/aab735

Palanisamy G, Bhuvaneswari K, Bharathi G et al (2018) Enhanced photocatalytic properties of ZnS–WO_3 nanosheet hybrid under visible light irradiation. ChemistrySelect 3:9422–9430. https://doi.org/10.1002/slct.201801688

Palanisamy G, Bhuvaneswari K, Chinnadurai A et al (2019) Magnetically recoverable multifunctional ZnS/Ag/$CoFe_2O_4$ nanocomposite for sunlight driven photocatalytic dye degradation and bactericidal application. J Phys Chem Solids. https://doi.org/10.1016/j.jpcs.2019.109231

Palareti G, Legnani C, Cosmi B et al (2016) Comparison between different D-Dimer cutoff values to assess the individual risk of recurrent venous thromboembolism: analysis of results obtained in the DULCIS study. Int J Lab Hematol 38:42–49. https://doi.org/10.1111/ijlh.12426

Pandiyan R, Mahalingam S, Ahn YH (2019) Antibacterial and photocatalytic activity of hydrothermally synthesized SnO_2 doped GO and CNT under visible light irradiation. J Photochem Photobiol B Biol 191:18–25. https://doi.org/10.1016/j.jphotobiol.2018.12.007

Patil SB, Bhojya Naik HS, Nagaraju G, Shiralgi Y (2018) Sugarcane juice facilitated eco-friendly synthesis of solar light active $CdFe_2O_4$ nanoparticles and its photocatalytic application. Eur Phys J Plus 133:229. https://doi.org/10.1140/epjp/i2018-12063-5

Phukan A, Bhattacharjee RP, Dutta DK (2017) Stabilization of SnO_2 nanoparticles into the nanopores of modified Montmorillonite and their antibacterial activity. Adv Powder Technol 28:139–145. https://doi.org/10.1016/j.apt.2016.09.005

Rashad MM, Ismail AA, Osama I et al (2014) Photocatalytic decomposition of dyes using ZnO doped SnO_2 nanoparticles prepared by solvothermal method. Arab J Chem 7:71–77. https://doi.org/10.1016/j.arabjc.2013.08.016

Ravichandran AT, Karthick R, Xavier AR et al (2017) Influence of Sm doped ZnO nanoparticles with enhanced photoluminescence and antibacterial efficiency. J Mater Sci Mater Electron 28:6643–6648. https://doi.org/10.1007/s10854-017-6355-2

Saleh NB, Khalid A, Tian Y et al (2019) Removal of poly- and perfluoroalkyl substances from aqueous systems by nano-enabled water treatment strategies. Environ Sci Water Res Technol 5:198–208. https://doi.org/10.1039/c8ew00621k

Sangchay W, Sikong L, Kooptarnond K (2012) Comparison of photocatalytic reaction of commercial P25 and synthetic TiO_2–AgCl nanoparticles. Procedia Eng 32:590–596. https://doi.org/10.1016/j.proeng.2012.01.1313

Sanoop PK, Anas S, Ananthakumar S et al (2016) Synthesis of yttrium doped nanocrystalline ZnO and its photocatalytic activity in methylene blue degradation. Arab J Chem 9:S1618–S1626. https://doi.org/10.1016/j.arabjc.2012.04.023

Senasu T, Hemavibool K, Nanan S (2018) Hydrothermally grown CdS nanoparticles for photodegradation of anionic azo dyes under UV–visible light irradiation. RSC Adv 8:22592–22605. https://doi.org/10.1039/c8ra02061b

Shanmugam V, Muppudathi AL, Jayavel S, Jeyaperumal KS (2018) Construction of high efficient g-C_3N_4 nanosheets combined with Bi_2MoO_6-Ag photocatalysts for visible-light-driven photocatalytic activity and inactivation of bacterias. Arab J Chem. https://doi.org/10.1016/j.arabjc.2018.05.009

Soltan WB, Lassoued MS, Ammar S, Toupance T (2017) Vanadium doped SnO_2 nanoparticles for photocatalytic degradation of methylene blue. J Mater Sci Mater Electron 28:15826–15834. https://doi.org/10.1007/s10854-017-7477-2

Sujatha K, Seethalakshmi T, Sudha AP, Shanmugasundaram OL (2019) Photocatalytic activity of pure, Zn doped and surfactants assisted Zn doped SnO_2 nanoparticles for degradation of cationic dye. Nano-Struct Nano-Objects 18:100305. https://doi.org/10.1016/j.nanoso.2019.100305

Suthakaran S, Dhanapandian S, Krishnakumar N, Ponpandian N (2019) Surfactants assisted SnO_2 nanoparticles synthesized by a hydrothermal approach and potential applications in water purification and energy conversion. J Mater Sci Mater Electron 30:13174–13190. https://doi.org/10.1007/s10854-019-01681-7

Teeparthi SR, Awin EW, Kumar R (2018) Dominating role of crystal structure over defect chemistry in black and white zirconia on visible light photocatalytic activity. Sci Rep 8:5541. https://doi.org/10.1038/s41598-018-23648-0

Vignesh S, Muppudathi AL, Sundar JK (2018) Multifunctional performance of gC_3N_4–$BiFeO_3$–Cu_2O hybrid nanocomposites for magnetic separable photocatalytic and antibacterial activity. J Mater Sci Mater Electron 29:10784–10801. https://doi.org/10.1007/s10854-018-9144-7

Vignesh S, Suganthi S, Kalyana Sundar J et al (2019a) Highly efficient visible light photocatalytic and antibacterial performance of PVP capped Cd:Ag: ZnO photocatalyst nanocomposites. Appl Surf Sci 479:914–929. https://doi.org/10.1016/j.apsusc.2019.02.064

Vignesh S, Suganthi S, Kalyana Sundar J, Raj V (2019b) Construction of α-Fe_2O_3/CeO_2 decorated g-C_3N_4 nanosheets for magnetically separable efficient photocatalytic performance under visible light exposure and bacterial disinfection. Appl Surf Sci 488:763–777. https://doi.org/10.1016/j.apsusc.2019.05.147

Wang J, Fan H, Yu H (2015) Synthesis of hierarchical porous Zn-doped SnO_2 spheres and their photocatalytic properties. J Mater Eng Perform 24:4260–4266. https://doi.org/10.1007/s11665-015-1745-1

Wang L, Wang Y, Su D, Zhao Y (2018) Enhancement of visible light photocatalytic activity over bistructural SnO_2 nanobelts. Superlattices Microstruct 114:416–420. https://doi.org/10.1016/j.spmi.2017.12.058

Wang X, Xu M, Liu L et al (2019) Effects specific surface area and oxygen vacancy on the photocatalytic properties of mesoporous F doped SnO_2 nanoparticles prepared by hydrothermal method. J Mater Sci Mater Electron. https://doi.org/10.1007/s10854-019-01981-y

Wu XF, Wang YJ, Song LJ et al (2019) A yolk–shell Bi@void@SnO_2 photocatalyst with enhanced tetracycline degradation. J Mater Sci Mater Electron 30:14987–14994. https://doi.org/10.1007/s10854-019-01871-3

Xin W, Zhu D, Liu G et al (2012) Synthesis and characterization of Mn-C-codoped TiO_2 nanoparticles and photocatalytic degradation of methyl orange dye under sunlight irradiation. Int J Photoenergy. https://doi.org/10.1155/2012/767905

Xu C, Ravi Anusuyadevi P, Aymonier C et al (2019) Nanostructured materials for photocatalysis. Chem Soc Rev 48:3868–3902. https://doi.org/10.1039/c9cs00102f

Yang L, Wang Z, Zhou X et al (2018) Synthesis of Pd-loaded mesoporous SnO_2 hollow spheres for highly sensitive and stable methane gas sensors. RSC Adv 8:24268–24275. https://doi.org/10.1039/c8ra03242d